PHYSICAL REVIEW B VOLUME 53, NUMBER 21 1 JUNE 1996-I

Theoretical studies of carrier transport in HgI_2

Yia-Chung Chang
Department of Physics, University of Illinois at Urbana-Champaign, 1110 West Green Street, Urbana, Illinois 61801

R. B. James
Department of Advanced Materials Research, Sandia National Laboratory, Livermore, California 94550

(Received 28 August 1995; revised manuscript received 14 February 1996)

Theoretical studies of the electron-phonon coupling and carrier mobility for red mercuric iodide are presented. The electronic states are calculated by an empirical pseudopotential method, while the lattice vibrations are described via a rigid-ion model. Effects due to the deformation potential and polar-optical scattering are discussed. Carrier mobilities along both c and a axes as functions of temperature are calculated and they are in good agreement with the experimental data. [S0163-1829(96)03821-0]

I. INTRODUCTION

Red mercuric iodide (HgI_2) is an important material for γ- and x-ray detectors. The electronic and phonon properties of HgI_2 are known fairly well due to recent theoretical studies.[1–4] A reliable description of the detailed electronic structures of the system was given by Turner and Harmon[1] via a relativistic linearized augmented plane-wave (RLAPW) calculation. We have recently reported an empirical nonlocal pseudopotential calculation of the electronic and optical properties of HgI_2 including the effects of the spin-orbit interaction.[2] The near-band-gap optical properties and effective masses obtained in this calculation are in good agreement with experimental data.[5–8]

The lattice vibrations of HgI_2 were studied by a rigid-ion model.[3,4] The model includes the long-range Coulomb interaction and short-range force constants up to second-nearest neighbors. An excellent fit to the available inelastic neutron scattering data[9] for six low-lying phonon branches as well as Raman scattering[10,11] and far-infrared[12] measurements for zone-center phonon modes was obtained.

There have been a great deal of experimental studies of transport properties of HgI_2.[13–17] However, a theoretical understanding of them is still lacking. A thorough review of carrier transport in HgI_2 can be found in Ref. 13. In this paper, we present theoretical studies of carrier transport in HgI_2. We have considered the scattering of electrons and holes from all possible phonon modes. The electron-phonon coupling is calculated based on the empirical pseudopotential model[2] for the electronic states and the rigid-ion model for the phonon modes.[4] It is found that polar-optical scattering is by far the strongest for low-energy carriers, and it is responsible for the low mobility observed experimentally. Our theoretical prediction for the intrinsic mobility as a function of temperature is in fairly good agreement with the experimental data.[14]

In Sec. II, we present the theory for the electron-phonon coupling of HgI_2. In Sec. III, we describe the theoretical predictions for the deformation potentials associated with various phonon modes of HgI_2. In Sec. IV, we describe the polar-optical scattering for noncubic crystals and examine the angular dependence of the electron-phonon coupling constant for HgI_2. In Sec. V, we discuss our calculated results for momentum relaxation rate and the carrier mobility. A summary of the paper is given in Sec. VI.

II. ELECTRON-PHONON COUPLING

In the rigid-ion model, the electron-phonon interaction is given by[18]

$$H_{\text{el -ph}} = -\sum_{\alpha\mathbf{R}} \frac{1}{\sqrt{NM_\alpha}} \sum_{\mathbf{q}j} Q_{\mathbf{q}j} e^{i\mathbf{q}\cdot\mathbf{R}} \hat{\epsilon}_\alpha^{(j)} \cdot \nabla V_\alpha(\mathbf{r}-\mathbf{R}-\tau_\alpha), \tag{1}$$

where N is the number of unit cells in the sample, α labels the different ions in a unit cell (two Hg's and four I's in the present case), M_α and τ_α denote the mass and position within a unit cell of ion α, $\mathbf{q}$ and $\hat{\epsilon}_\alpha^{(j)}$ denote the wave vector and polarization vector at position τ_α of phonon mode j, and V_α describes the pseudopotential for an electron interacting with ion α. $Q_{\mathbf{q}_j}$ is the normal mode coordinate of mode j which takes the second quantization form

$$Q_{\mathbf{q}_j} = \sqrt{\frac{\hbar}{2\omega_{\mathbf{q}_j}}} (a_{\mathbf{q}_j}^\dagger + a_{\mathbf{q}_j}),$$

where $\omega_{\mathbf{q}_j}$ denotes the frequency of mode j.

A schematic diagram of the unit cell of HgI_2 can be found in Ref. 3. Note that the solid has inversion symmetry about the midpoint between the two Hg atoms in a unit cell. If we choose the point as the origin of the coordinate system, the atomic positions of the two Hg atoms are $(-a/4,-a/4,-c/4)$ and $(a/4,a/4,c/4)$, and those of the four I atoms are $(-a/4,a/4,-0.111c)$, $(a/4,-a/4,0.111c)$, $(-a/4,a/4,0.389c)$, and $(a/4,-a/4,-0.389c)$. Here, $a=4.37$ Å and $c=12.44$ Å. We adopt a coordinate system in which the z axis is parallel to the c axis.

The local pseudopotentials of the mercury and iodine have the form

$$V_L(\mathbf{q}) = a_1(q^2-a_2)/(e^{a_3(q^2-a_4)}+1), \tag{2}$$

0163-1829/96/53(21)/14200(12)/$10.00

and the nonlocal pseudopotentials have the form

$$V_{\mathrm{NL}}(\mathbf{K},\mathbf{K}')=4\pi\sum_l (2l+1)P_l(\cos\theta)\times\int drr^2V_l(r)j_l(Kr)j_l(K'r)/\Omega_a\,, \tag{3}$$

where $\cos\theta=\mathbf{K}\cdot\mathbf{K}'/KK'$, Ω_a is the atomic volume, P_l is a Legendre polynomial, j_l is a spherical Bessel function, and $V_l(r)=A_le^{-(r/R)^2}$. We use $R=2.3a_B$, where a_B is the Bohr radius. $a_i(i=1,2,3,4)$ and $A_l(l=0,1)$ are adjustable parameters which are tabulated in Ref. 2.

The matrix element of $H_{\text{el-ph}}$ between two electronic states with wave vectors $\mathbf{k}$ and $\mathbf{k}'$ is given by

$$\langle\mathbf{k}'|H_{\text{el-ph}}|\mathbf{k}\rangle=-i\sum_\alpha\sqrt{\frac{\hbar}{2\omega_{\mathbf{q}j}NM_\alpha}}\sum_{\mathbf{q}j,\mathbf{G},\mathbf{G}'}\Delta(\mathbf{k}'-\mathbf{k}\mp\mathbf{q})\hat{\epsilon}_\alpha^{(j)}\cdot(\mathbf{K}'-\mathbf{K})C^*_{\mathbf{k}'}(\mathbf{G}')C_{\mathbf{k}}(\mathbf{G})\times[V_L^{(\alpha)}(\mathbf{K}'-\mathbf{K})+V_{\mathrm{NL}}^{(\alpha)}(\mathbf{K},\mathbf{K}')]e^{-i(\mathbf{K}'-\mathbf{K})\cdot\tau_\alpha}/N_a\,, \tag{4}$$

where $\mathbf{K}=\mathbf{k}+\mathbf{G}$ and $\mathbf{G}$ denotes a reciprocal lattice vector. $C_{\mathbf{k}}(G)$ is the expansion coefficient for the electronic eigenstate of the pseudopotential Hamiltonian in terms of plane waves. N_a is the number of atoms per unit cell,

$$\Delta(\mathbf{k}'-\mathbf{k}\mp\mathbf{q})=\delta_{\mathbf{k}',\mathbf{k}\pm\mathbf{q}+\mathbf{G}}\,,$$

which means that the momentum is conserved with or without the help of a reciprocal lattice vector $\mathbf{G}$. Since we are only concerned with transport properties of Γ-valley electrons (or holes), the umklapp process ($\mathbf{G}\neq 0$) can be ignored. The $+(-)$ sign in the above equation denotes a phonon absorption (emission) process.

In a deformation potential model appropriate for acoustic phonons, the electron-phonon interaction is described by

$$H_{\text{el-ph}}=\frac{1}{\sqrt{NM_{\text{cell}}}}\sum_{\mathbf{q}j}Q_{\mathbf{q}j}e^{i\mathbf{q}\cdot\mathbf{r}}\hat{\epsilon}\cdot\mathbf{q}\Xi_d\,, \tag{5}$$

where Ξ_d is the deformation potential associated with pure dilation and M_{cell} denotes the total mass per unit cell. One can generalize the above form to an optical phonon labeled with j by defining a coupling coefficient $D_0^{(j)}$ such that

$$H_{\text{el-ph}}=\sum_\alpha\frac{1}{\sqrt{NM_{\text{cell}}}}\sum_{\mathbf{q}j}Q_{\mathbf{q}}e^{i\mathbf{q}\cdot\mathbf{r}}D_0^{(j)}(\mathbf{q}). \tag{6}$$

For longitudinal optical-phonons $D(\mathbf{q})$ is approximately independent of q for small q, while for acoustical phonons, we have the simple relation

$$D_0(\mathbf{q})=\hat{\epsilon}\cdot\mathbf{q}\Xi_d\,.$$

The matrix element between two electronic states in this model can be written as

$$\langle\mathbf{k}'|H_{\text{el-ph}}|\mathbf{k}\rangle=-i\sqrt{\frac{\hbar}{2\omega_{qj}NM_{\text{cell}}}}\sum_{\mathbf{q}}\delta_{\mathbf{k}',\mathbf{k}\pm\mathbf{q}}D_0^{(j)}(\mathbf{q})I(\mathbf{k}',\mathbf{k}), \tag{7}$$

where

$$I(\mathbf{k}',\mathbf{k})\equiv\sum_G C^*_{\mathbf{k}'}(G')C_{\mathbf{k}}(G)$$

denotes an overlap integral.

Comparing Eq. (7) with Eq. (4), we can define the effective coupling coefficient as

$$\begin{aligned}D(\mathbf{q})&\equiv D_0^{(j)}(q)I(\mathbf{k}',\mathbf{k})\\&=\Bigg|\sum_\alpha\sqrt{\frac{M_{\text{cell}}}{M_\alpha}}\sum_{j,\mathbf{G},\mathbf{G}'}\hat{\epsilon}_\alpha^{(j)}\cdot(\mathbf{K}'-\mathbf{K})C^*_{\mathbf{k}'}(\mathbf{G}')\\&\quad\times C_{\mathbf{k}}(\mathbf{G})[V_L^{(\alpha)}(\mathbf{K}'-\mathbf{K})\\&\quad+V_{\mathrm{NL}}^{(\alpha)}(\mathbf{K},\mathbf{K}')]e^{-i(\mathbf{K}'-\mathbf{K})\cdot\tau_\alpha}/N_a\Bigg|,\end{aligned} \tag{8}$$

where $\mathbf{K}=\mathbf{k}+\mathbf{G}$ and $\mathbf{q}=\pm(\mathbf{k}'-\mathbf{k})$.

In a scattering event, both energy and momentum should be conserved, i.e.,

$$\mathbf{k}'=\mathbf{k}\pm\mathbf{q}$$

and

$$E_{\mathbf{k}'}=E_{\mathbf{k}}\pm\hbar\omega_q\,,$$

where $E_{\mathbf{k}}$ is the energy of electron at wave vector $\mathbf{k}$, and $\mathbf{q}$ is the wave vector of a phonon absorbed or emitted. For acoustical phonons whose deformation potentials are of primary interest, the typical frequencies are less than 0.1 THz which correspond to energies less than 0.4 meV. Thus, the following relation approximately holds:

$$\mathbf{k}'=-\mathbf{k}=\pm\mathbf{q}/2, \tag{9}$$

since $E_{-\mathbf{k}}=E_{\mathbf{k}}$ as a consequence of time reversal. For optical phonons, the frequencies are between 0.5 and 4.5 THz (with energies from 2 to 18 meV) for HgI_2, and the above relation is not quite valid. However, since the electron-phonon coupling for high-frequency optical-phonons is insensitive to **k** and **q** near the zone center, the result obtained this way is still adequate.

To understand the behavior of these coupling constants, we must first examine the symmetry properties of phonons in HgI_2. The point group of the system is D_{4h} which contains elements E, σ_1, σ_2, S_1, S_2, S_3, $\sigma_2 S_1$, and $S_1\sigma_2$, where E is the identity, $\sigma_1(\sigma_2)$ is a reflection about the y-z (x-z) plane, S_1 is a 90° rotation about the z axis followed by a reflection about the x-y plane, $S_2=S_1^2$, and $S_3=S_1^3$. The group theory analysis for HgI_2 structure has been reported in Ref. 19. The phonon dispersion curves of all 18 branches were shown in Fig. 3 of Ref. 4. The phonon branches are labeled by their space group representations according to the notation of Ref. 19. There are three irreducible representations $\Lambda_1,\Lambda_3,\Lambda_5$ for **q** along the [001] direction (Γ to Z). The Λ_5 representation is two dimensional, indicating transverse modes, whereas the Λ_1 and Λ_3 representations are one dimensional, indicating longitudinal modes. For **q** along [100] (Γ to X), there are four irreducible representations $\Delta_1,\Delta_2,\Delta_3,\Delta_4$ (all one dimensional). The Δ_2 and Δ_3 modes contain symmetric and antisymmetric sums of y displacements associated with atoms related by inversion, namely, those labeled by 1 and 2, 3 and 6, or 4 and 5 (see Fig. 1 of Ref. 3); hence, they are transverse modes. The Δ_4 modes contain admixture of $x-$ and $z+$ components, while the Δ_1 modes contain admixture of symmetric sum of x displacements (denoted $x+$ component).

The symmetries of zone-center modes are labeled according to the point group representations (Ref. 12). The E (E_g or E_u) modes are twofold degenerate when the wave vector approaches zero from the c axis. They correspond to vibrations along the x and y directions. The A (A_{1g} or A_{2u}) and B (B_{1g} or B_{2u}) modes are singlefold, corresponding to vibrations along the z axis. The subscripts g (gerade) and u (ungerade) denote even and odd parity modes with respect to the inversion center. A schematic diagram for atomic displacement in modes of various symmetries can be found in Fig. 1 of Ref. 12.

In our calculation, the spin-orbit interaction is included for the electron band structures. Thus, each band is doubly degenerate due to Kramers degeneracy. In our calculation, we sum over the final spin index and average over the initial spin index. Namely, we replace the intraband coupling matrix element in Eqs. (4) and (7) by

$$\langle \mathbf{k}'|H_{\text{el-ph}}|\mathbf{k}\rangle=\left(\frac{1}{2}\sum_{s,s'}|\langle \mathbf{k}',s'|H_{\text{el-ph}}|\mathbf{k},s\rangle|^2\right)^{1/2},$$

where s,s' sum over the two Kramers degenerate states.

Using Eqs. (8) and (9), we have calculated the effective coupling coefficient $D(\mathbf{q})$ as a function of q. The deformation-potential coupling is nonzero only for longitudinal phonon modes (i.e., with Λ_1 or Λ_3 symmetry for **q** along [001] and Δ_1 or Δ_4 symmetry for **q** along [100]). At the zone center ($\mathbf{q}=0$), only the A_{1g} mode (totally symmetric with respect to all point operations) has nonzero coupling coefficient. This is because we have only considered intraband scattering here, in which case the initial and final states are the same and the electron can only scatter with a totally symmetric mode. The results for (a) the lowest conduction band (C1), (b) the heavy-hole band (HH), and (c) the light-hole band (LH) are shown in Fig. 1. The three solid (dotted) curves labeled 1–3 in the left panels are associated with the three Λ_1 (Λ_3) modes ordered according to their frequencies. Similarly, the six solid (dotted) curves labeled 1–6 in the

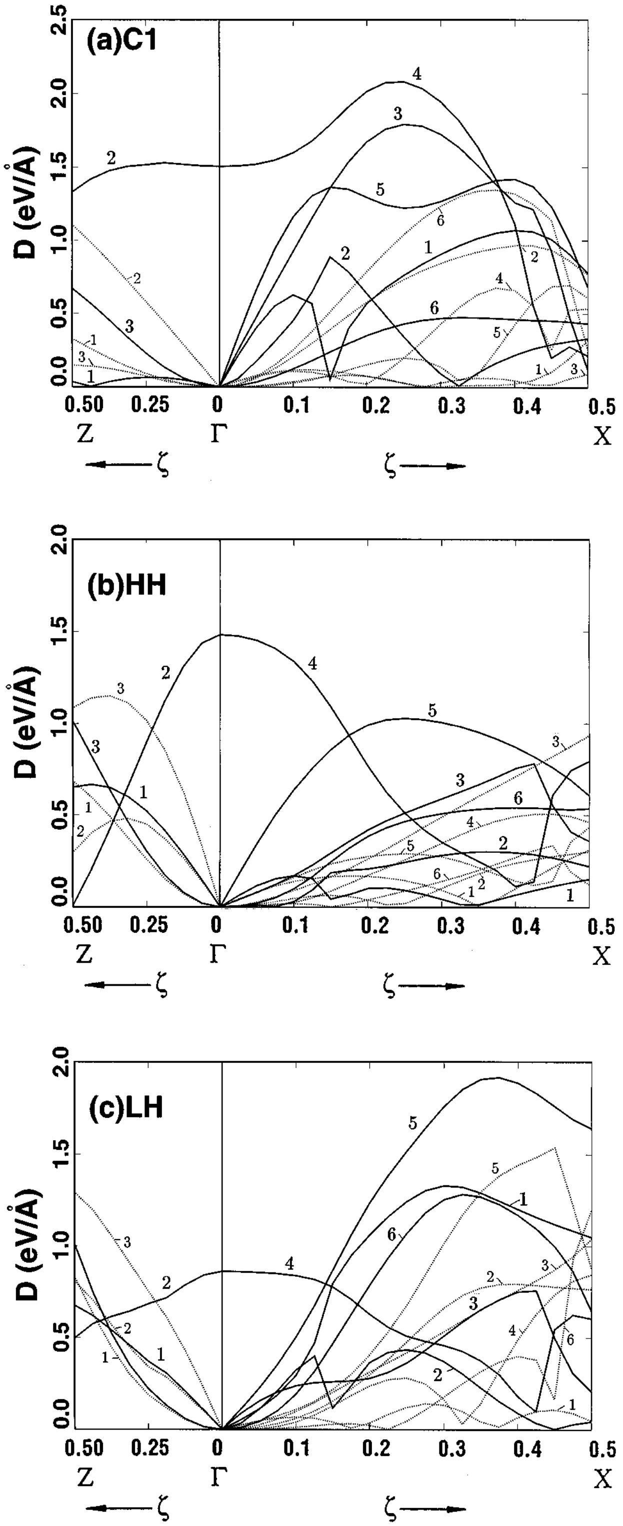

FIG. 1. Electron-phonon coupling coefficients as a function of phonon wave vector for (a) the lowest conduction band (C1), (b) the heavy-hole band (HH), and (c) the light-hole band (LH).

right panels are associated with the six Δ_1 (Δ_4) modes ordered according to their frequencies. The first Λ_1 and $\Delta_1(\Delta_4)$ modes correspond to the longitudinal acoustical branch along the *c* and *a* axes, respectively.

The second Λ_1 mode and the fourth Δ_1 mode merge into the A_{1g} mode at the zone center. The A_{1g} mode (a breathing mode) creates a lattice vibration that preserves the point symmetry of the crystal; thus, the electronic energy will suffer a change even when $q=0$. As shown in Fig. 1, $D(\mathbf{q})$ is finite at the zone center only for this mode.

III. DEFORMATION POTENTIALS

Since HgI_2 has six atoms per unit cell, there exist 15 optical branches in addition to the three acoustical branches. For acoustic branches and for some optical branches, the effective electron-phonon coupling constant D($\mathbf{q}$) is linear in q for small q. We then define effective deformation potentials as

$$\Xi^*(\theta_q)=D(\mathbf{q})/q,$$

where θ_q is the polar angle of q with respect to the z axis (c axis). Due to the fact that the crystal is noncubic, there is in general a θ_q dependence in the deformation potential. We examine the angular dependence of the deformation potential by calculating $\Xi^*(\theta_q)=D(\mathbf{q})/q$ at $q=0.02$ Å^{-1} with θ_q varying from zero to $\pi/2$. The angular dependence is quite complicated due to the mixing of several modes with similar frequencies. However, for modes with similar frequencies, we can simply add up their corresponding coupling coefficients squared and use the square root of the sum to represent the net effect of all these nearly degenerate modes.

Following the elastic theory of Herring and Vogt,[20] the θ_q dependences of the acoustical-phonon deformation potentials for anisotropic systems are fitted by polynomials of $\cos^2\theta_q$,

$$\Xi_L^*(\theta_q)=\Xi_d^*+\Xi_r^*\cos^2\theta_q+\Xi_s^*\cos^4\theta_q \qquad (10)$$

for longitudinal modes and by

$$\Xi_T^*(\theta_q)=\Xi_u^*\sin\theta_q\cos\theta_q \qquad (11)$$

for transverse modes. These expressions would allow the scattering rates to be calculated analytically.

Figure 2 shows the angular dependence of the deformation potential $\Xi^*(\theta_q)$ for the longitudinal acoustical (LA) and transverse acoustical (TA) modes. The solid curves are calculated results and the dotted curves are fitted results obtained by using Eq. (10) for the LA mode and Eq. (11) for the TA modes. The parameters Ξ_d^*, Ξ_r^*, Ξ_s^*, and Ξ_u^* used for the fit are listed in Table I.

From Fig. 2, we find that the angular dependence of the effective deformation potentials for the LA mode are indeed well described by the simple analytic expressions given in Eq. (10). For the TA mode, the fit to Eq. (11) is rather poor. Here, we choose the maximum values of fitted $\Xi^*(\theta_q)$ to be the same as the actually calculated ones, with a displaced peak positions in θ_q. Thus, when we integrate over θ_q to obtain the total scattering rate, the deviation becomes insignificant. Furthermore, since average value of $\Xi^*(\theta_q)$ for the TA mode is much smaller than that for the LA mode, such a poor fit will not alter the final acoustical-phonon scattering rate in which the LA mode dominates.

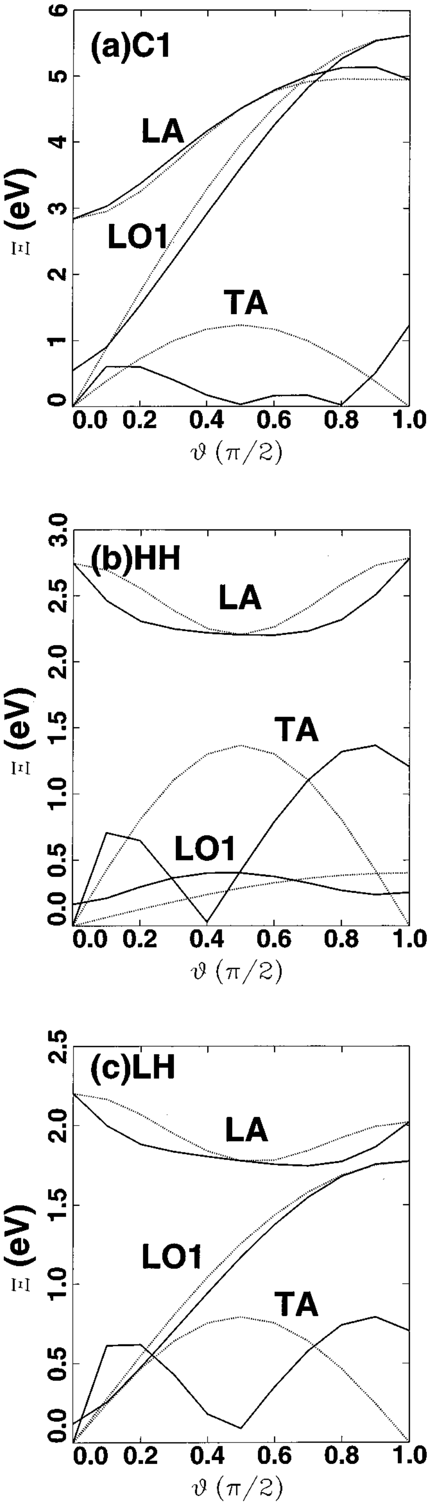

FIG. 2. Angular dependence of the effective deformation potential for (a) the lowest conduction band (C1), (b) the heavy-hole band (HH), and (c) the light-hole band (LH). Solid curves: calculated based on Eq. (8). Dotted curves: calculated based on Eqs. (9), (10), and (14).

As we mentioned in the previous section there is only one

TABLE I. Effective deformation potentials Ξ_d^*, Ξ_u^*, and Ξ_1^* and the coupling coefficient D_0 for the optical-phonon for the conduction (C1), heavy-hole (HH), and light-hole (LH) bands. All deformation potentials are in units of eV and D_0 is in units of eV/Å.

Band	Ξ_d^*	Ξ_r^*	Ξ_s^*	Ξ_u^*	Ξ_1^*	D_0
C1	4.95	0.376	-2.49	2.45	5.62	1.50
HH	2.79	-2.29	2.25	2.74	0.404	1.49
LH	2.02	-1.16	1.33	1.59	1.77	0.87

TABLE II. Effective masses (in units of free electron mass) and their ratios for the conduction (C1), heavy-hole (HH), and light-hole (LH) bands.

	C1	HH	LH
m_l^*	0.37^a	2.06^b	0.60^a
m_t^*	0.29^a	1.03^b	0.60^a

[a] Obtained by the empirical pseudopotential method (EPM) as described in Ref. 2.

[b] Bloch *et al.* (Ref. 6).

optical mode with A_{1g} symmetry whose coupling coefficient $D(\mathbf{q})$ is finite at $q=0$. Thus it contributes to the zeroth-order optical-phonon scattering. If we approximate both $D(\mathbf{q})$ and $\omega(q)$ for the A_{1g} mode by constant values D_0 and ω_0 corresponding to their respective values at $q=0$, we obtain the scattering rate as[21]

$$W(E_{\mathbf{k}})=(\pi D_0^2/\rho\omega_0)\{n(\omega_0)N(E_{\mathbf{k}}+\hbar\omega_0)+[n(\omega_0)+1]N(E_{\mathbf{k}}-\hbar\omega_0)\}, \tag{12}$$

where ρ is the mass density,

$$E_{\mathbf{k}}=\frac{\hbar^2(k_x^2+k_y^2)}{2m_t^*}+\frac{\hbar^2k_z^2}{2m_l^*}$$

is the carrier energy, $N(E)=(2m_l^*m_t^{*2}E)^{1/2}/4\pi^2\hbar^3$ is the carrier density of states for a given spin, and $n(\omega_0)$ is the phonon population given by

$$n(\omega_0)=(e^{\hbar\omega_0/k_BT}-1)^{-1}.$$

For all other 14 optical branches, the deformation potential constant vanishes at $q=0$. However, several modes have appreciable deformation potential at finite q. We shall add the contributions to $[D(\mathbf{q})]^2$ for all modes with frequencies higher than 2 THz (which include the Λ_1 and Λ_3 modes labeled by 2 and 3 and the Δ_1 and Δ_4 modes labeled by 4–6) and define the net contribution as $D_0(q)$. The net contribution becomes even less q dependent near the zone center. Therefore, Eq. (12) becomes a better approximation for describing optical-phonon scattering when we consider the net effect of all optical branches with high frequencies. We shall use Eq. (12) to calculate the net contribution of these higher-lying optical modes to the scattering rate with the coupling coefficient D_0 given in Table I and $\omega_0/2\pi=3.352$ THz.

For those optical branches (i.e., the seven lower-lying optical modes) with frequencies substantially lower than ω_0, they also have appreciable contribution to the scattering rate. The frequencies of these modes are ranging from 0.6 THz to 1.1 THz near the zone center (see Fig. 4 of Ref. 4). We shall show below that the angular dependence of the deformation potential can be approximately written as

$$\Xi_1^*(\theta_q)=\Xi_1^*\sin\theta_q. \tag{13}$$

The angular dependence of the effective deformation potential representing the net effect of these modes (denoted LO1) is plotted in Fig. 2 for (a) the lowest conduction band (C1), (b) the heavy-hole band (HH), and (c) the light-hole band (LH). The solid curves are calculated results and the dotted curves are fitted results obtained by using Eq. (13). The parameter Ξ_1^* used for the fit is listed in Table I. We find that the angular dependence of the effective deformation potentials for the LO1 modes is indeed well described by the simple analytic expression given in Eqs. (13). With this simple expression, the scattering rate is given by

$$\begin{aligned}W_1(\mathbf{k})=\frac{\Xi_1^{*2}}{8\pi^2\rho\omega_1}\int q^2\sin^2\theta_q\{&n(\omega_1)\delta_{\mathbf{k}',\mathbf{k}+\mathbf{q}}\\&\times\delta(E_{\mathbf{k}'}-E_{\mathbf{k}}-\hbar\omega_1)\\&+[n(\omega_1)+1]\delta_{\mathbf{k}',\mathbf{k}-\mathbf{q}}\\&\times\delta(E_{\mathbf{k}'}-E_{\mathbf{k}}+\hbar\omega_1)\}d\mathbf{k}'d\mathbf{q}.\end{aligned} \tag{14}$$

Carrying out the integral we obtain

$$\begin{aligned}W_1(\mathbf{k})=\frac{\Xi_1^{*2}m_t^{*2}\sqrt{2m_l^*}}{\pi\rho\omega_1\hbar^5}\{&n(\omega_1)\sqrt{E_{\mathbf{k}}+\hbar\omega_1}\\&\times[\tfrac{2}{3}(E_{\mathbf{k}}+\hbar\omega_1)+u_k]\\&+[n(\omega_1)+1]\sqrt{E_{\mathbf{k}}-\hbar\omega_1}\\&\times[\tfrac{2}{3}(E_{\mathbf{k}}-\hbar\omega_1)+u_k]\},\end{aligned} \tag{15}$$

where m_l^* and m_t^* are the longitudinal and transverse effective masses as listed in Table II, $u_k\equiv\hbar^2(k_x^2+k_y^2)/2m_t^*$, and $\omega_1/2\pi=0.868$ THz is the average frequency of the optical-phonons of interest.

IV. POLAR-OPTICAL SCATTERING

In addition to deformation potentials, the ions with opposite charges vibrating against each other give rise to a long-range macroscopic electric field. The interaction of a carrier with such field is known as the polar-optical scattering (or Frölich scattering).[22] In HgI_2, there exist three optical modes (labeled by E_u^1, E_u^2, and A_{2u}^1) which lead to a nonzero dipole moment. As a result, these modes are infrared active and possess angular dispersion at $\mathbf{q}$ near zero (see Fig. 4 of Ref. 4). The electron-phonon interaction due to polar-optical scattering associated with mode j is given by

$$H_{\text{el-ph}}=\frac{1}{\sqrt{NM_{\text{cell}}}}\sum_{\mathbf{q},\alpha}\sqrt{\frac{M_{\text{cell}}}{M_\alpha}}\frac{e}{v_c}\frac{e_\alpha^*\hat{\epsilon}_\alpha^{(j)}\cdot\hat{q}}{\epsilon(\infty)}\left(\frac{4\pi q}{q^2+q_0^2}\right)Q_{\mathbf{q}j}e^{i\mathbf{q}\cdot\mathbf{r}}, \tag{16}$$

where e is the free electron charge, e_α^* is the effective dynamic charge of ion α, $\epsilon(\infty)$ is the high-frequency dielectric constant, $\hat{\epsilon}_\alpha^{(j)}$ is the polarization vector, v_c is volume of the unit cell, and q_0 is the reciprocal Debye screening length (which depends on the free carrier concentration). The effective dynamic charge e_α^* is defined as $|\partial M/\partial u|$, where u is the relative displacement and M is the corresponding electric moment. For noncubic crystals, e_α^* should be different for different directions of the applied electric field. The parallel and perpendicular components of e_α^* can be related to the longitudinal and transverse phonon frequencies defined as zeros and poles of $\epsilon(\omega)$ of the three infrared active modes by[28]

$$4\pi(N/V)\sum_\alpha \frac{e_\alpha^{*2}}{M_\alpha}=\epsilon(\infty)\sum_j (\omega_{jL}^2-\omega_{jT}^2).$$

Their values, determined by reflectivity measurements, are $e_l^*=2.27e$ and $e_t^*=3.06e$ for the Hg ion.[12] Here the subscript $l(t)$ indicates parallel (perpendicular) to the c axis. For the I ion, the charge neutrality gives $e_{\mathrm{I}}^*=-\frac{1}{2}e_{\mathrm{Hg}}^*$. In the rigid-ion model,[3] the anisotropy for both the dynamic charge and dielectric constant is ignored, and it is found that[4] $e^{*2}/\epsilon(\infty)=0.266$ for the I ion. Using $\epsilon_l(\infty)=5.2$ and $\epsilon_t(\infty)=5.45$ and the experimental values for e_l^* and e_t^* (see Ref. 12), we obtain $e_l^{*2}/\epsilon_l(\infty)=0.248$ and $e_t^{*2}/\epsilon_t(\infty)=0.429$ for the I ion. The rigid-ion model prediction turns out to be quite close to the experimental result for the electric field along the c axis. It should be pointed out here that the effective dynamic charge appears to be too large compared with that inferred from the first-principles calculation.[1] If we write the total longitudinal polarization (including contribution from ions and valence electrons) as[23]

$$\mathbf{P}_{\mathbf{l}}=\sum_\alpha e_{l\alpha}^*\mathbf{u}_\alpha,$$

where $\mathbf{u}_\alpha$ denotes the displacement vector for atom α, then $e_{l\alpha}^*=e_\alpha^*/\epsilon(\infty)$ corresponds to the effective charge introduced by Callen[24] in the diatomic case. This effective charge is a measure of the ionicity and its value for I in HgI_2 is around $-0.25e$, indicating that the material is more covalent than ionic, consistent with the prediction given in Ref. 1. Comparing Eq. (17) with Eq. (6), the effect of polar-optical scattering can be described by a q-dependent coupling coefficient with

$$D_j^*(\mathbf{q})=\left|\sum_\alpha \sqrt{\frac{M_{\mathrm{cell}}}{M_\alpha}}\frac{e}{v_c}\frac{e_\alpha^*\hat{\epsilon}_\alpha^{(j)}\cdot\hat{q}}{\epsilon(\infty)}\right|\left(\frac{4\pi q}{q^2+q_0^2}\right)$$
$$\equiv C_j(\theta_q)\left(\frac{q}{q^2+q_0^2}\right). \tag{17}$$

Using the displacement vectors obtained by the rigid-ion model,[4] we can obtain the angular-dependent coefficients $C_j(\theta_q)$ for the E_u^1,E_u^2, and A_{2u}^1 modes. To include the anisotropy effect, we simply replace $e_\alpha^*\hat{\epsilon}_\alpha^{(j)}\cdot\hat{q}/\epsilon(\infty)$ in Eqs. (16) and (17) by

$$\left[\frac{e_{\alpha,l}^*\hat{\epsilon}_{\alpha,l}^{(j)}}{\epsilon_l(\infty)}+\frac{e_{\alpha,t}^*\hat{\epsilon}_{\alpha,t}^{(j)}}{\epsilon_t(\infty)}\right]\cdot\hat{q}. \tag{18}$$

In Fig. 3, we plot the angular dependent coupling coefficient C_j for the three infrared active optical branches (E_u^1,E_u^2, and A_{2u}^1). The solid curves are results obtained by using Eq. (17) and the isotropic effective dynamic charge predicted by the rigid-ion model[4] and a spherical dielectric constant $\epsilon(\infty)=5.2$. The dotted curves are results obtained by using the anisotropic expression (18) and the low-temperature experimental values[12] for $e_{l,t}^*$ and $\epsilon(\infty)$.

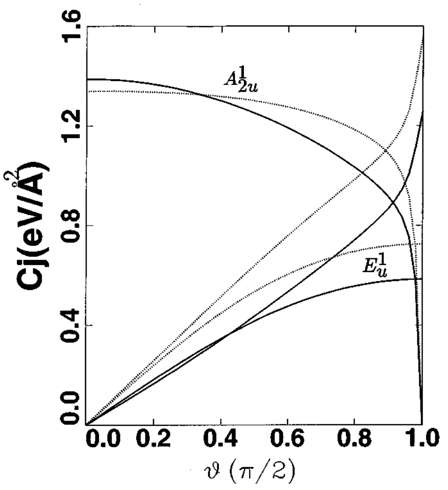

FIG. 3. Angular dependence of the coupling coeficient for polar-optical-phonon scattering for the three infrared-active modes. Solid curves: with isotropic dynamic charge as given in Ref. 4. Dotted curves: with anisotropic dynamic charges as given in Ref. 12.

The scattering rate due to polar-optical-scattering associated with mode j is given by

$$W_j(\mathbf{k})=\frac{1}{8\pi^2\rho}\int\frac{C_j^2(\theta_q)q^2}{\omega_j(\theta_q)(q^2+q_0^2)^2}\{n(\omega_j(\theta_q))\delta_{\mathbf{k}',\mathbf{k}+\mathbf{q}}$$
$$\times\delta(E_{\mathbf{k}'}-E_{\mathbf{k}}-\hbar\omega_j(\theta_q))+[n(\omega_j)+1]\delta_{\mathbf{k}',\mathbf{k}-\mathbf{q}}$$
$$\times\delta(E_{\mathbf{k}'}-E_{\mathbf{k}}+\hbar\omega_j)\}d\mathbf{k}'d\mathbf{q}. \tag{19}$$

In this paper, we are only interested in low carrier concentrations so that q_0 in Eq. (14) can be neglected. For $\mathbf{k}$ along a general direction, including the anisotropy of band structure and phonon dispersion is complicated. We therefore adopt a spherical approximation in which we ignore the angular dependence of the phonon dispersion $\omega_j(\theta_q)$, and we define new variables

$$q_i^*=\sqrt{\sigma}q_i \quad \text{for } i=x,y$$

and $q_z^*=q_z$, where $\sigma\equiv m_l^*/m_t^*$, and similarly for $\mathbf{k}^*(\mathbf{k}'^*)$, so that $E_{\mathbf{k}}(E_{\mathbf{k}'})$ becomes a spherical function of $\mathbf{k}^*(\mathbf{k}'^*)$. Equation (19) becomes

TABLE III. Spherical averages of the coupling coefficients C_j for polar-optical scatterings associated with the E_u^1, E_u^2, and A_{2u}^1 modes calculated by the rigid-ion model and by using experimental values for effective dynamic charges (in parentheses). All coefficients are in units of eV/Å^2. The optimum frequencies $\overline{\omega_j}$ used in Eq. (29) in units of THz are included in parentheses following the band symmetry label.

Band	E_u^1(1.078)	E_u^2(3.549)	A_{2u}^1(4.035)
C1	0.460(0.580)	0.626(0.832)	1.115(1.190)
HH	0.427(0.539)	0.573(0.766)	1.089(1.153)
LH	0.478(0.601)	0.655(0.869)	1.126(1.208)

$$W_j(\mathbf{k})=\frac{1}{8\pi^2\rho}\int\frac{C_j^2(\theta_q)}{\omega_j {q^*}^2(\sin^2\theta_q^*/\sigma+\cos^2\theta_q^*)}$$
$$\times\{n(\omega_j)\,\delta_{\mathbf{k}^{*\prime},\mathbf{k}^*+\mathbf{q}^*}\,\delta(E_{\mathbf{k}'}-E_{\mathbf{k}}-\hbar\omega_j)$$
$$+[n(\omega_j)+1]\,\delta_{\mathbf{k}^{*\prime},\mathbf{k}^*-\mathbf{q}^*}$$
$$\times\,\delta(E_{\mathbf{k}'}-E_{\mathbf{k}}+\hbar\omega_j)\}d\mathbf{q}^*d\mathbf{k}^{*\prime}/\sigma, \tag{20}$$

where $\cos\theta_q^*\equiv q_z^*/q^*$. Furthermore, we replace $C_j^2(\theta_q)/(\sin^2\theta_q^*+\sigma\cos^2\theta_q^*)$ by a spherically averaged coupling constant $\overline{C_j^2}$ defined by

$$\overline{C_j^2}=\int_{-1}^{1}\frac{C_j^2(\theta_q)}{\sin^2\theta_q^*+\sigma\cos^2\theta_q^*}\,d\cos\theta_q^*/2. \tag{21}$$

Carrying out the integral in Eq. (19) we obtain[21]

$$W_j(\mathbf{k})=\frac{\overline{C_j^2}}{2\pi\rho\hbar\omega_j\upsilon_k}\left\{n(\omega_j)\sinh^{-1}\sqrt{\frac{E_{\mathbf{k}}}{\hbar\omega_j}}\right.$$
$$\left.+[n(\omega_j)+1]\sinh^{-1}\sqrt{\frac{E_{\mathbf{k}}}{\hbar\omega_j}-1}\right\}, \tag{22}$$

where $\upsilon_k=\hbar k^*/m_l^*=\sqrt{2E_{\mathbf{k}}/m_l^*}$. The spherically averaged coupling constants as defined in Eq. (21) are listed in Table III.

TABLE IV. Coefficients for transport parameters for acoustical phonons as given in Eqs. (21) and (22). The abbreviations $c^*=c_{11}-c_{12}-2c_{44}$, $c_l=c_{12}+2c_{44}+\frac{3}{5}c^*$, and $\overline{c}=(c_{44}+\frac{1}{2}c^*)(c_{44}+\frac{1}{3}c^*)$ have been used. The integrals I_n and J_n are the same as defined in Ref. 20.

ξ_l	$I_0+(c^*/c_l)(-0.15I_0+1.5I_2-1.75I_2)$
η_l	$2I_1+(c^*/c_l)(-0.3I_1+3I_2-3.5I_3$
ζ_l	$I_2+(c^*/c_l)(-0.15I_2+1.5I_3-1.75I_4)$
ξ_l'	$\frac{c_l(c_{44}+5c^*/6)}{\overline{c}}(I_1-I_2)-\frac{c^*c_l}{\overline{c}}(I_2-I_3)$
η_l'	$2I_3+(c^*/c_l)(-0.3I_3+3I_4-3.5I_5)$
ζ_l'	$2I_4+(c^*/c_l)(-0.3I_4+3I_5-3.5I_6)$
$\xi_t,\eta_t,\zeta_t,$ ξ_t',η_t',ζ_t'	same as parallel cases above but with $\frac{1}{2}J_n$ replacing each I_n

V. MOMENTUM RELAXATION RATES AND MOBILITY

To calculate the carrier mobility, we also need the momentum relaxation time τ_i (the subscript i denotes the direction of transport) which is related to the scattering rate via the expression[20,25]

$$\frac{1}{\tau_i(E)}=\int k_i(k_i-k_i')W(\mathbf{k}',\mathbf{k})d\mathbf{k}'\,\delta(E-E_{\mathbf{k}})d\mathbf{k}\;\Big/\int k_i^2\,\delta(E-E_{\mathbf{k}})d\mathbf{k}, \tag{23}$$

where $W(\mathbf{k}',\mathbf{k})$ denotes the scattering rate from state $\mathbf{k}$ to $\mathbf{k}'$.

The momentum relaxation rates for acoustical phonons with deformation potentials described by Eqs. (10) and (11) can be worked out analytically similar to the theory of Herring and Vogt[20] and we obtain

$$\frac{1}{\tau_l(E)}=(2\pi/\hbar c_L)\frac{3}{4}[\xi_l\Xi_d^{*2}+\eta_l\Xi_d^*\Xi_r^*$$
$$+\zeta_l(\Xi_r^{*2}+2\Xi_d^*\Xi_s^*)+\xi_l'\Xi_u^{*2}$$
$$+\eta_l'\Xi_r^*\Xi_s^*+\zeta_l'\Xi_s^{*2}]k_BTN(E) \tag{24}$$

for transport parallel to the c axis and

$$\frac{1}{\tau_t(E)}=(2\pi/\hbar c_L)\frac{3}{4}[\xi_t\Xi_d^{*2}+\eta_t\Xi_d^*\Xi_r^*$$
$$+\zeta_t(\Xi_r^{*2}+2\Xi_d^*\Xi_s^*)+\xi_l'\Xi_u^{*2}+\eta_t'\Xi_r^*\Xi_s^*$$
$$+\zeta_t'\Xi_s^{*2}]k_BTN(E) \tag{25}$$

for transport perpendicular to the c axis. Here E is the energy of the carrier, $c_L=c_{12}+2c_{44}+\frac{3}{5}(c_{11}-c_{12}-2c_{44})$ is the average elastic constant, k_B is the Boltzmann constant, and T is the temperature. $\xi_{l,t},\eta_{l,t},\ \zeta_{l,t},\ \xi_{l,t}',\eta_{l,t}'$, and $\zeta_{l,t}'$ are constants depending on the effective mass ratio $\sigma\equiv m_l^*/m_t^*$ and the elastic constants c_{11}, c_{12}, and c_{44}. Explicit expressions for these constants are given in Table IV and their values for HgI_2 are listed in Table V. The elastic constants used are (in units of 10^{11} dyn cm^{-2}) $c_{11}=3.16$ (Ref. 9), $c_{12}=0.559$ (Ref.

TABLE V. Transport parameters for acoustical phonons of HgI_2.

Band	ξ_l	η_l	ζ_l	ξ_l'	η_l'	ζ_l'	ξ_t	η_t	ζ_t	ξ_t'	η_t'	ζ_t'
C1	1.322	1.647	0.603	0.435	1.501	0.399	1.338	0.628	0.145	0.393	0.224	0.051
HH	1.297	1.797	0.724	0.376	1.829	0.478	1.343	0.783	0.203	0.420	0.353	0.083
LH	1.333	1.566	0.548	0.447	1.096	0.340	1.333	0.551	0.118	0.371	0.170	0.038

27), and $c_{44}=0.727$ (Ref. 9). Note that in the above equations we have used the equipartition approximation, i.e.,

$$n(\omega_q)=(e^{\hbar\omega_q/k_BT}-1)^{-1}\approx\frac{k_BT}{\hbar\omega_q}.$$

This is a good approximation, since at room temperature, we have $\hbar\omega_q/k_BT\ll 1$.

For zeroth-order optical-phonon scattering, one can show that $1/\tau=W(k)$ as given in Eq. (12) because the coupling coefficient is independent of $\mathbf{q}$ and the angular average of the term proportional to k_ik_i' in Eq. (19) vanishes.[21] For the first-order optical-phonon scattering, we obtain

$$\frac{1}{2\tau_t(E)}=\frac{1}{\tau_l(E)}=\frac{\Xi_1^{*2}m_t^{*2}\sqrt{2m_l^*}}{\pi\rho\omega_1\hbar^5}\times n(\omega_1)\sqrt{E+\hbar\omega_1}\left[\tfrac{2}{3}(E+\hbar\omega_1)+\tfrac{2}{5}E\right]+[n(\omega_1)+1]\sqrt{E-\hbar\omega_1}\left[\tfrac{2}{3}(E-\hbar\omega_1)+\tfrac{2}{5}E\right].\tag{26}$$

Note that τ_t^{-1} is twice as large as τ_l^{-1}. This is due to the fact that $\Xi_1^*(q)=\Xi_1^*\sin\theta_q$ which suppressed the scattering along the c axis.

To calculate the momentum relaxation rate for polar-optical scattering, we set $q_0=0$. This is valid for the low carrier concentration ($<10^{14}\ \mathrm{cm}^{-3}$) considered here. Substituting Eq. (17) into Eq. (20) we obtain

$$\frac{1}{\tau_l(E)}=\frac{3\hbar^3}{16\pi^2\rho(2m_l^*E)^{3/2}}\sum_j\int_{-k_m}^{k_m}dk_zk_z\int d\phi_q^*\int_0^{\pi}d\theta_q^*\,\frac{C_j^2(\theta_q)\cos\theta_q^*\sin\theta_q^*}{\omega_j(\sin^2\theta_q^*+\sigma\cos^2\theta_q^*)}\times\{-n(\omega_j)[q_+^{(1)}/R_+(q_+^{(1)})+q_+^{(2)}/R_+(q_+^{(2)})]+[n(\omega_j)+1][q_-^{(1)}/R_-(q_-^{(1)})+q_-^{(2)}/R_-(q_-^{(2)})]\},\tag{27}$$

$$\frac{1}{\tau_t(E)}=\frac{3\hbar^3}{32\pi^2\rho(2m_l^*E)^{3/2}}\sum_j\int_{-k_m}^{k_m}(k_m^2-k_z^2)^{1/2}dk_z\int d\phi_q^*\int_0^{\pi}d\theta_q^*\,\frac{C_j^2(\theta_q)\sin^2\theta_q^*\cos\phi_q^*}{\omega_j(\sin^2\theta_q^*+\sigma\cos^2\theta_q^*)}\times\{-n(\omega_j)[q_+^{(1)}/R_+(q_+^{(1)})+q_+^{(2)}/R_+(q_+^{(2)})]+[n(\omega_j)+1][q_-^{(1)}/R_-(q_-^{(1)})+q_-^{(2)}/R_-(q_-^{(2)})]\},\tag{28}$$

where $k_m=\sqrt{2m_l^*E}/\hbar$, $R_\pm(q)=(\hbar^2/m_l^*)|q\pm(k_z\cos\theta_q^*+(k_m^2-k_z^2)^{1/2}\sin\theta_q^*\cos\phi_q^*)|$. $q_\pm^{(1)}$ and $q_\pm^{(2)}$ are two positive real roots of the equation

$$\frac{\hbar^2}{2m_l^*}[q^2\pm 2q(k_z\cos\theta_q^*+(k_m^2-k_z^2)^{1/2}\sin\theta_q^*\cos\phi_q^*)]=\pm\hbar\omega_j.$$

Here θ_q^* is the polar angle of $\mathbf{q}^*$ with respect to the c axis and ϕ_q^* is the azimuthal angle between $\mathbf{q}^*$ and $\mathbf{k}$.

If we replace $C_j^2(\theta_q)/(\sin^2\theta_q^*+\sigma\cos^2\theta_q^*)$ by its spherically averaged value and $\omega_j(\theta_q)$ by its value at the angle where $C_j(\theta_q)$ is peaked, the above results reduce to[21]

$$\frac{1}{\tau(E)}=\frac{\overline{C_j^2}}{4\pi\rho\hbar\overline{\omega_j}v_E}\left\{n(\overline{\omega_j})\left[\sqrt{1+\frac{\hbar\overline{\omega_j}}{E}}-\frac{\hbar\overline{\omega_j}}{E}\sinh^{-1}\sqrt{\frac{E}{\hbar\overline{\omega_j}}}\right]\right\}+\left\{[n(\overline{\omega_j})+1]\left[\sqrt{1-\frac{\hbar\overline{\omega_j}}{E}}+\frac{\hbar\overline{\omega_j}}{E}\sinh^{-1}\sqrt{\frac{E}{\hbar\overline{\omega_j}}-1}\right]\right\},\tag{29}$$

where $v_E=\sqrt{2E/m_l^*}$. The values of $\overline{\omega_j}$ [$=\omega_j(\pi/2)$ for the E_u^1 and E_u^2 modes and $\omega_j(0)$ for the A_{1u} mode] are listed in Table III.

Using Eqs. (24)–(29) and Tables I–V, we can calculate the momentum relaxation rates due to both deformation-potential and polar-optical scatterings. Figure 4 (Fig. 5) shows the results for the electron (hole) at (a) 300 K and (b) 77 K. For simplicity, the polar-optical scattering rates were calculated in the spherical model [Eq. (29)]. In Fig. 4, the three peak structures for the polar-optical scattering are due to the onset of the optical-phonon emission at the phonon energies for modes E_u^1, E_u^2, and A_{2u}^1, with the E_u^1 mode being the strongest, since it has much lower phonon energy compared with the other two modes and $1/\tau$ is inversely proportional to ω_j [see Eq. (29)]. In Fig. 5, both the heavy-hole and light-hole contributions are included. The light-hole contribution starts at hole energy of 0.2 eV which corresponds to the heavy-hole and light-hole splitting at the zone center (see, Ref. 2). We note that the polar-optical scattering dominates the other scatterings for carrier energies less than 0.1 eV, and it becomes comparable to the sum of all other scattering rates at carrier energies around 0.5 eV. For carriers with energies higher than 0.5 eV, the deformation-potential scattering becomes more important. However, for high-

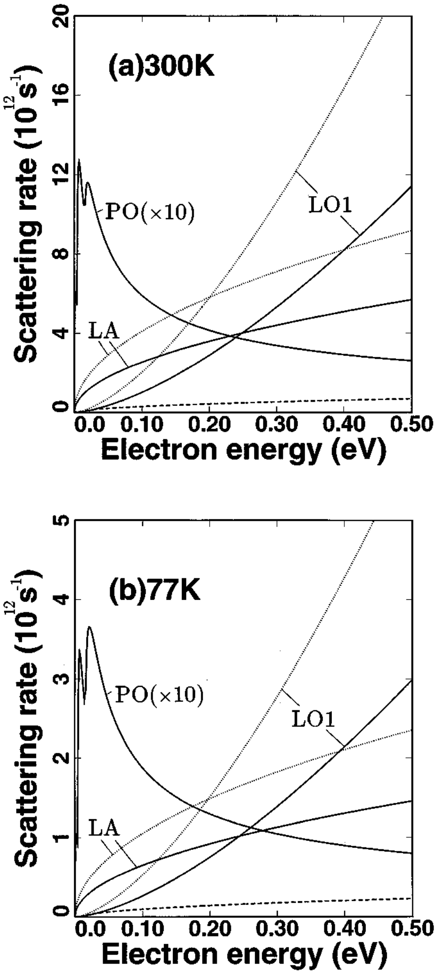

FIG. 4. Momentum relaxation rates associated with various phonon branches at (a) 300 K and (b) 77 K as functions of the electron energy for the lowest conduction band. The polar-optical-phonon rates have been scaled down by a factor 10. Solid curves: parallel to the c axis. Dotted curves: perpendicular to the c axis. Dashed curve: LO deformation potential scattering (isotropic).

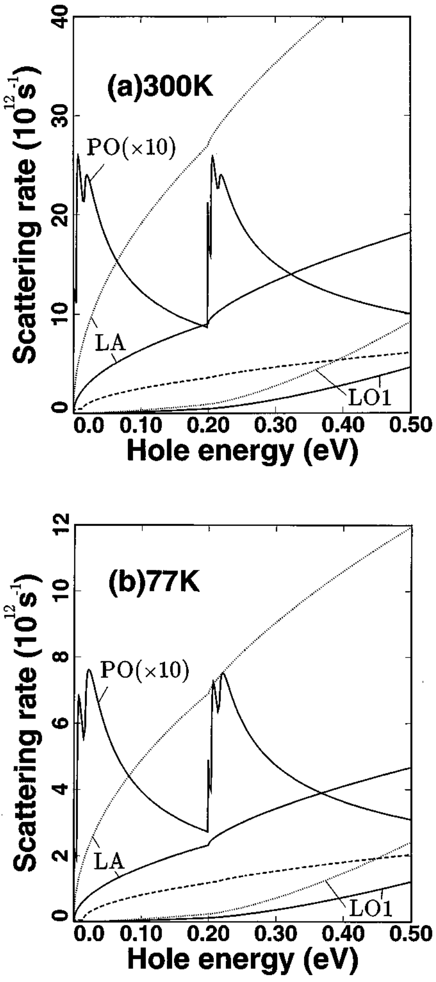

FIG. 5. Momentum relaxation rates associated with various phonon branches at (a) 300 K and (b) 77 K as functions of the hole energy for the heavy-hole band. The polar-optical-phonon rates have been scaled down by a factor 10. Solid curves: parallel to the c axis. Dotted curves: perpendicular to the c axis. Dashed curve: LO deformation potential scattering (isotropic).

energy carriers, the scattering with large-momentum phonons becomes important, and the deformation potential approximation adopted here which assumes that $D(q)$ is proportional to q will be invalidated. In addition, the deformation potentials for interband scattering as well as intervalley scattering also need to be considered.

The anisotropy in the momentum relaxation rate due to polar-optical scattering is also examined based on Eqs. (27) and (28). The results for the electron (hole) are shown in Fig. 6 (Fig. 7) for (a) $T=300$ K and (b) $T=77$ K. The solid (dotted) curves are for $\tau_l^{-1}(\tau_t^{-1})$. Also shown in these figures are the results (dash-dotted curves) obtained by using the spherical-model expression [Eq. (29)]. For both the electron and hole, the anisotropy is quite large with τ_t^{-1} larger than τ_l^{-1} by about a factor between 1.5 and 2. We can understand this behavior by examining Fig. 3 in which we find that C_j is zero at $\theta=0$ (parallel to c axis) and large at $\theta=\pi/2$ (perpendicular to c axis) for the E_u^1 and E_u^2 modes. This enhances the scattering rates perpendicular to the c axis.

Finally the mobilities are related to the momentum relaxation times via[20]

$$\mu_l=\frac{e}{m_l^*}\frac{\langle E\tau_l(E)\rangle}{\langle E\rangle},$$

$$\mu_t=\frac{e}{m_t^*}\frac{\langle E\tau_t(E)\rangle}{\langle E\rangle},$$

where $\langle\ \rangle$ denotes a thermal average with a Boltzmann distribution in the nondegenerate limit. To calculate the mobility, we use the momentum relaxation rates for deformation potential as obtained above. To simplify the calculation, we use the spherical-model expression [Eq. (29)] for the polar-optical scattering, but scale it by appropriate factors to take into account the anisotropy for the electron. As shown in Fig. 6, τ_l^{-1} and τ_t^{-1} differ from the spherical results $(1/\tau)$ approximately by an energy-independent factor. We find $\tau_l^{-1}\approx 0.821\tau^{-1}$ and $\tau_t^{-1}\approx 1.281\tau^{-1}$ for the electron. For the hole, we find $\tau_l^{-1}\approx 0.734\tau^{-1}$ and $\tau_t^{-1}\approx 1.335\tau^{-1}$. Figures 8 and 9 show the mobility as a function of temperature for the electron and hole, respectively. The results are in fairly good

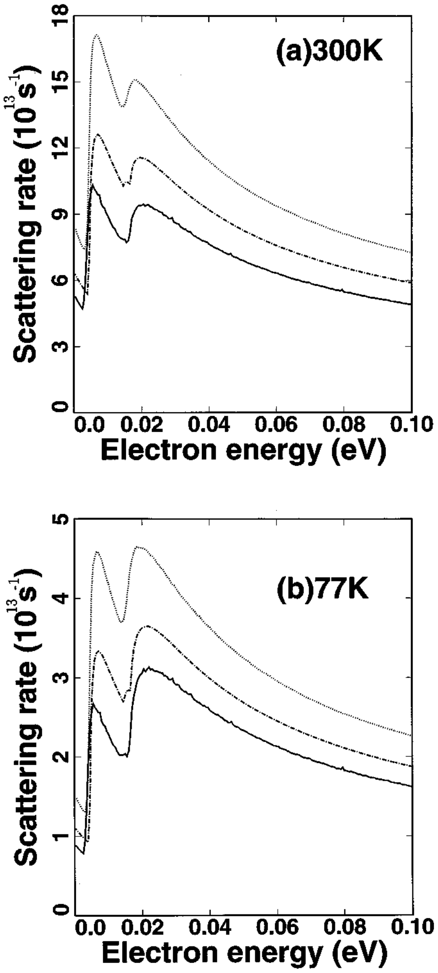

FIG. 6. Momentum relaxation rates associated with polar-optical scattering at (a) 300 K and (b) 77 K as functions of the electron energy for the lowest conduction band. Solid curves: τ_l^{-1}. Dotted curves: τ_t^{-1}. Dot-dashed curve: τ^{-1} (spherical model).

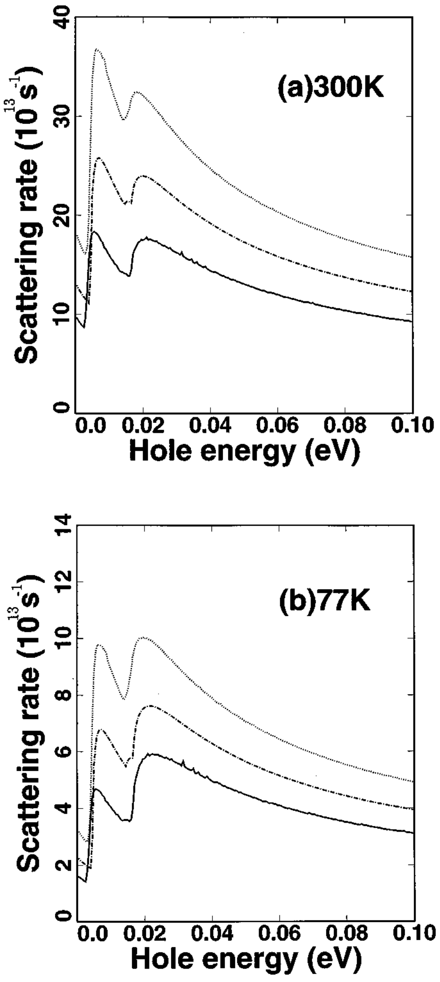

FIG. 7. Momentum relaxation rates associated with polar-optical scattering at (a) 300 K and (b) 77 K as functions of the hole energy for the heavy-hole band. Solid curves: τ_l^{-1}. Dotted curves: τ_t^{-1}. Dot-dashed curve: τ^{-1} (spherical model).

agreement with the experimental data taken by Minder *et al.*,[14,15] indicating that the intrinsic scattering mechanism plays a major role in the observed mobility. Table VI shows a comparison between our theoretical predictions and experimental data for the mobilities at 200 and 300 K. The calculated mobilities are in general within a factor of 2 of the experimental values. The discrepency may be attributed to the uncertainty in the effective masses and dynamic charges used. We predict that the electron mobility is higher for transport parallel to the c axis than that perpendicular to the c axis for all temperatures, while the opposite is true for the hole mobility. This qualitative difference is consistent with experimental data and it can be explained with our theoretical analysis. For the electron transport, the polar-optical scattering rate perpendicular the c axis is about 1.6 times that parallel to the c axis (see Fig. 7) and the longitudinal to transverse effective mass ratio is 1.276; thus the combined effect favors the mobility parallel to the c axis. For the hole transport, the polar-optical scattering rate perpendicular the c axis is about 1.8 times that parallel to the c axis (see Fig. 7) and the logitudinal to transverse effective mass ratio is 2.0, which causes the mobility parallel to the c axis to be slightly

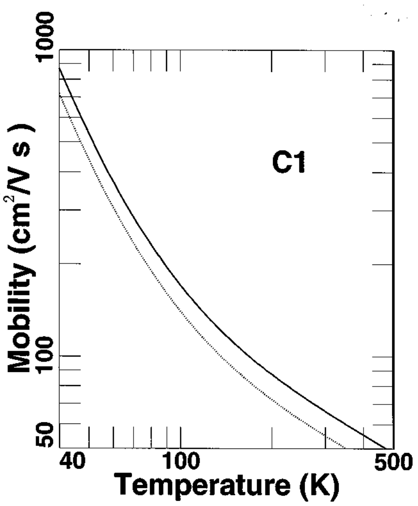

FIG. 8. Electron mobilities as functions of temperature. Solid (dotted) curve is for transport parallel (perpendicular) to the c axis.

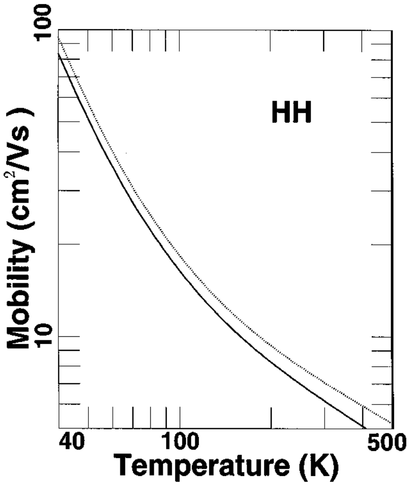

FIG. 9. Hole mobilities as functions of temperature. Solid (dotted) curve is for transport parallel (perpendicular) to the *c* axis.

smaller than that perpendicular to the *c* axis. Experimentally, the ratio of longitudinal to transverse mobility (μ_l/μ_t) is about 1.4 for the electron and 0.5 for the hole for temperatures below 200 K.[13] The corresponding values obtained here is 1.2 and 0.85, respectively. The discrepency is most likely caused by the uncertainty in the values of effective masses used here. Had we used different hole effective masses such that the ratio m_l^*/m_t^* is 4.2 as suggested by the first-principles calculation,[1] then the calculated mobility ratio (μ_l/μ_t) would have been about 0.5, in good agreement with data. It should be noted that HgI_2 undergoes a structural phase transition (from α to β phase) at a temperature around 427 K.[26] Thus, our theoretical predictions for the mobilities at temperatures beyond 427 K should not be taken seriously.

VI. CONCLUSION

We have presented detailed theoretical studies of the carrier-phonon scattering due to all possible phonon modes. It is found that the polar-optical phonon scattering dominates the transport properties for low-energy carriers which are of common interest. For the electron, the mobility along the *c* axis is slightly higher than that perpendicular to the *c* axis, while for the hole the reverse is true. This qualitative difference is explained by the anisotropy in the momentum relaxation rate and the large anisotropy in the hole effective mass. The calculated results for both electron and hole mobilities are in good agreement with the experiment (within a factor of 2) when the sample is sufficiently pure where the intrinsic scattering dominates. The discrepency between theory and transport data is most likely caused by the uncertainty in the input values of effective masses and dynamic charges used in the calculation. The uncertainty in the phonon polarization vectors calculated by the rigid-ion model can be another source of error, since the empirical phonon model contains a large number of adjustable parameters. On the other hand, since the polar-optical phonons dominate transport and their polarization vectors are largely determined by the dynamic charges and symmetry, the error introduced by the nonuniqueness of short-range parameters should be small. Namely, the angular dependence of the electron-phonon coupling and hence the anisotropy in scattering rates obtained this way should be fairly reliable. By comparing the anisotropy in calculated and measured mobilities, we conclude that the longitudinal to transverse effective mass ratio for the hole should be around 4, in agreement with the first-principles calculation of Ref. 1. Although the deformation-potential scattering is found to be relatively unimportant in determining the mobility for HgI_2, it will play an important role in the analysis of Raman and photoluminescence spectra of HgI_2.

TABLE VI. Comparison between theory and experiment on the carrier mobilities of HgI_2 (in units of cm^2/V sec).

Temperature		μ_l^e	μ_t^e	μ_l^h	μ_t^h
200 K	Theory	88	72	8.2	9.3
	Experiment	145[a]	90[b]	10[a]	
300 K	Theory	67	55	6.2	7.1
	Experiment	100[a]	65[b]	4[a]	23[c]

[a] Minder *et al.* (Ref. 14).
[b] Minder *et al.*. (Ref. 15).
[c] Manfredotti *et al.* (Ref. 16).

ACKNOWLEDGMENT

This work is supported in part by the U.S. Department of Energy.

---

[1] D. E. Turner and B. N. Harmon, Phys. Rev. B **40**, 10 516 (1989).
[2] Y. C. Chang and R. B. James, Phys. Rev. B **46**, 15 040 (1992).
[3] Y. C. Chang, H. K. Sim, and R. B. James, in *Semiconductors for Room Temperature Radiation Detector Application*, edited by R. B. James, T. E. Schlesinger, P. Siffert, and L. Franks, MRS Symposia Proceedings No. 302 (Materials Research Society, Pittsburgh, 1993), p. 121.
[4] H. K. Sim, Y. C. Chang, and R. B. James, Phys. Rev. B **49**, 4559 (1994).
[5] K. Kanzaki and I. Imai, J. Phys. Soc. Jpn. **32**, 1003 (1972).
[6] P. D. Bloch, J. W. Hodby, C. Schwab, and D. W. Stacey, J. Phys. C **11**, 2579 (1978).
[7] T. Goto and A. Kasuya, J. Phys. Soc. Jpn. **50**, 520 (1981).
[8] A. Anedda, F. Raga, E. Grilli, and M. Guzzi, Nuovo Cimento **38**, 439 (1977).
[9] B. Prevot, C. Schwab, and B. Dorner, Phys. Status Solidi B **88**, 327 (1978).
[10] S. Nakashima and Z. M. Balkanski, Phys. Rev. B **34**, 5801 (1986).
[11] N. Kuroda, T. Iwabuchi, and Y. Nishina, J. Phys. Soc. Jpn. **52**, 2419 (1983).
[12] J. Biellmann and B. Prevot, Infrared Physics, **20,** 99 (1979).
[13] X. J. Bao, T. E. Schlesinger, and R. B. James, in *Semicoductors and Semimetals*, edited by T. E. Schlesinger and R. B. James (Academic Press, San Diego, 1995), Vol. 43, Chap. 4.
[14] R. Minder, G. Majni, C. Canali, G. Ottaviani, R. Stuck, J. P.

Ponpon, C. Schwab, and P. Siffert, J. Appl. Phys. **45**, 5074 (1974).

[15] R. Minder, G. Ottaviani, and C. Canali, J. Phys. Chem. Solids **37**, 417 (1976).

[16] C. Manfredotti, R. Murri, and L. Vasanelli, Solid State Commun. **21**, 53 (1977).

[17] P. D. Bloch, J. W. Hodby, T. E. Jenkins, D. W. Stacey, and C. Schwab, Nuovo Cimento B **38**, 337 (1977).

[18] O. Madelung, *Introduction to Solid State Theory* (Springer-Verlag, New York, 1978), Chap. 4.

[19] M. Sieskind, J. Phys. Chem. Solids **39**, 1251 (1978).

[20] C. Herring and E. Vogt, Phys. Rev. **101**, 944 (1956).

[21] B. K. Ridley, *Quantum Process in Semiconductors* (Oxford University Press, New York, 1982).

[22] H. Frölich, Proc. R. Soc. London A **160**, 230 (1937).

[23] T. Kurosawa, J. Phys. Soc. Jpn. **16**, 1298 (1961).

[24] H. Callen, Phys. Rev. **76**, 1394 (1949).

[25] This expression is valid for elastic scattering for anisotropic band and for both elastic and inelastic scaterings for isotropic band. For inelastic scattering and anisotropic band, the expression is not quite valid. In our case, however, since the dominant optical-phonon (E_u^1) mode has an energy (~ 3 meV) much smaller than the average electron (hole) energy at room temperature (~ 26 meV), the scattering is almost elastic. So we expect that the use of this expression will not lead to significant error.

[26] J. B. Newkirk, Acta Metall. **4**, 316 (1956).